nature communications

Article

https://doi.org/10.1038/s41467-025-58670-0

Mechanistic understanding of UvrA damage detection and lesion hand-off to UvrB in Nucleotide Excision Repair

Received: 30 September 2024

Accepted: 28 March 2025

Published online: 10 April 2025

Check for updates

Marianna Genta[1], Giulia Ferrara[1], Riccardo Capelli[2], Diego Rondelli[2], Sarah Sertic[2], Martino Bolognesi[2,3], Menico Rizzi[1], Franca Rossi[1], David Jeruzalmi[4], Antonio Chaves-Sanjuan[2,3] ✉ & Riccardo Miggiano[1] ✉

Nucleotide excision repair (NER) represents one of the major molecular machineries that control chromosome stability in all living species. In Eubacteria, the initial stages of the repair process are carried out by the UvrABC excinuclease complex. Despite the wealth of structural data available, some crucial details of the pathway remain elusive. In this study, we present a structural investigation of the *Mycobacterium tuberculosis* UvrAUvrB complex and of the UvrA dimer, both in complex with damaged DNA. Our analyses yield insights into the DNA binding mode of UvrA, showing an unexplored conformation of Insertion Domains (IDs), underlying the essential role of these domains in DNA coordination. Furthermore, we observe an interplay between the ID and the UvrB Binding Domain (UBD): after the recognition of the damage, the IDs repositions with the concomitant reorganization of UBD, allowing the formation of the complex between UvrA and UvrB. These events are detected along the formation of the uncharacterized $UvrA_2UvrB_1$-DNA and the $UvrA_2UvrB_2$-DNA complexes which we interpret as hierarchical steps initiating the DNA repair cascade in the NER pathway, resulting in the formation of the pre-incision complex.

Nucleotide excision repair (NER) is a versatile and highly conserved DNA repair pathway responsible for removing bulky DNA-distorting adducts[1]. In bacteria, two proteins, namely UvrA and UvrB, serve as the initial NER damage sensors[1–5]. UvrA is an ATPase in the ATP-binding cassette (ABC) superfamily that functions as a dimer. The catalytic core of each protomer of the functional $UvrA_2$ homodimer consists of two composite nucleotide-binding domains (NBD-I and NBD-II) and each moiety contain an ATP/ADP binding site (ATP-I and ATP-II, belonging to NBD-I and NBD-II, respectively) and a Signature domain (SIG-I and SIG-II belonging to NBD-I and NBD-II, respectively). Two distinctive extra domains sprout from the NBD-I of UvrA: the UvrB Binding Domain (UBD) and the Insertion Domain (ID)[6–10] (Fig. 1a). UvrB is annotated as a member of the SF2 helicase family for the presence of conserved helicase motifs (I-VI); it contains the classical RecA-like domains (domains 1a and 3), in addition to three auxiliary domains (domains 1b, 2, and 4) and the β-hairpin motif that projects from domain 1a[11–15].

There is consensus on the distinct roles of the two proteins in the early damage detection process: UvrA acts as the primary sensor of DNA double-helix deformation[13,16], with the capacity to simultaneously bind damaged DNA and UvrB, behaving as a molecular matchmaker that enables the precise delivery of UvrB to the lesioned site[13,17]. The discrimination of the lesion and subsequent stable binding represents the first step of the UvrA activity; the binding of UvrB is then the functional prerequisite for the complete pathway to proceed to the pre-incision complex formation, with one UvrB molecule bound to

[1]Department of Pharmaceutical Sciences, University of Piemonte Orientale, Via Bovio 6, 28100 Novara, Italy. [2]Department of Biosciences, University of Milan, Milan 20133, Italy. [3]Pediatric Clinical Research Center Romeo ed Enrica Invernizzi and NOLIMITS, University of Milan, Milan 20133, Italy. [4]Department of Chemistry and Biochemistry, The City College of New York, New York, NY 10031, USA. ✉e-mail: antonio.chaves@unimi.it; riccardo.miggiano@uniupo.it

the lesion. Subsequently, UvrC nuclease cleaves the DNA on both sides of the damaged site, the UvrD helicase removes the excised oligonucleotide, and DNA polymerase I fills the gap. Finally, DNA ligase I seals the nick (Fig. 1b).

Despite the amount of available structural information[5–8,10,11,18,19], some critical molecular and structural aspects of the initial steps of bacterial NER remain unclear. In particular, although atomic structures of UvrA bound to damaged DNA[7] and UvrA bound to UvrB[5] have been reported, a description of the configuration of the UvrA-UvrB complex bound to DNA is still lacking.

Specifically, the conformational changes occurring in UvrA during genome scanning and the overall architecture of the lesion-sensing complex remain elusive[9]. On the one hand, it has been proposed that UvrA can locate and verify the DNA lesion independently of UvrB[16,20,21]. On the other hand, forming an UvrA-UvrB complex has been suggested as the bona fide DNA damage-detecting step, initiating the NER pathway[5,9,18,22]. The precise oligomerization state of the UvrA-UvrB complex remains unclear since the in vitro stoichiometry has been alternatively estimated as $UvrA_2UvrB_2$ or $UvrA_2UvrB_1$[5,13,20–22]. Indeed, it is possible that both forms could populate the NER pathway. UvrA is essential for damage identification, sensing DNA helix distortion and participating in DNA melting and unwinding[23,24]. However, whether it is UvrA alone or in complex with UvrB the one responsible for the damage recognition mechanism remains to be established. Moreover, two other outstanding questions regarding the transition toward the pre-incision complex remain to be addressed. First, the only available $UvrA_2UvrB_2$ structural model[5] is symmetric, with the two UvrB molecules capable of binding complementary strands. However, the pre-incision complex is asymmetric and contains a single copy of UvrB[25]. It is, therefore, unclear how the lesion-containing strand is identified. Second, the $UvrA_2UvrB_2$ places UvrB ~80 Å from the damage site. Two mechanisms have been hypothesized to explain the localization of UvrB to the lesion: the "recruitment model" model, which suggests a direct delivery of UvrB on the lesion through $UvrA_2UvrB_2$ complex reconfiguration, and the "translocation model", which implies that UvrA dissociates before the translocation of UvrB to the damage site; UvrB translocates using its intrinsic ATPase activity[5,12].

Our study focuses on the NER pathway in *Mycobacterium tuberculosis* (MTB), which is essential to maintaining infectivity and survival[4,26,27]. Using cryogenic electron microscopy (cryo-EM), we determined three distinct macromolecular complexes in the MTB NER pathway: $UvrA_2$ bound to DNA (*Mt*$UvrA_2$-DNA), the $UvrA_2$-$UvrB_2$ complex bound to DNA (*Mt*$UvrA_2UvrB_2$-DNA), and a previously undescribed $UvrA_2$-$UvrB_1$ complex bound to DNA (*Mt*$UvrA_2UvrB_1$-DNA). Our structural, genetic, and biochemical study came to several conclusions. UvrA in the *Mt*$UvrA_2$-DNA complex was found in a distinct configuration compared to a prior structure. Notably, the two IDs are observed clamping on DNA as they mediate the melting and unwinding of the duplex. We suggest a division of labor between the two UvrA protomers. In the *Mt*$UvrA_2UvrB_1$-DNA complex, we establish a link between UvrB binding to a particular UvrA monomer and the concomitant release of this monomer's ID from contact with DNA. The structure of the *Mt*$UvrA_2UvrB_2$-DNA complex reveals how the repositioning of UvrA's IDs may enable the transfer of the lesion to UvrB. We propose that the three structures (*Mt*$UvrA_2$-DNA, *Mt*$UvrA_2UvrB_1$-DNA, and *Mt*$UvrA_2UvrB_2$-DNA) operate sequentially in the NER pathway.

Results

*Mt*UvrA dimer copurifies with endogenous *E. coli* dsDNA containing oxidative damage

The *Mt*UvrA-*Mt*UvrB complex (prepared as previously described[6,11]) was vitrified and cryo-EM data were collected using a Talos Arctica (Suppplementary Table 1). The 2D average analysis revealed the presence of particles consistent with the UvrA dimer, but not compatible with the complex (Supplementary fig. 1). Surprisingly, during the 3D reconstruction step, two distinct sets of particles were identified, corresponding to the DNA-free *Mt*$UvrA_2$ and to *Mt*$UvrA_2$ in complex with dsDNA; these were subsequently processed to achieve a final resolution of 4.9 Å and 4.2 Å, respectively (Supplementary fig. 1, Supplementary Table 1 and Supplementary fig. 2a, b). The structure of *Mt*$UvrA_2$-DNA was reconstructed at higher resolution and will be discussed in a later section, while the structural analysis of *Mt*$UvrA_2$ without DNA is part of the supplementary information.

A posteriori analyses revealed contaminant nucleic acids in the *Mt*UvrA sample used in cryo-EM (Supplementary fig. 3a, b). Given the nature of UvrA as DNA damage detector, we sought to identify the type of lesion possibly present in the copurified DNA. To this end, we conducted a dot blot-based analysis using antibodies specific to prevalent types of DNA lesion, that confirmed the presence of oxidized nucleobases (i.e. 8-oxoguanine), while common UV-induced adducts (i.e. CPDs and 6-4PP) were absent (Supplementary fig. 3c). Taking into account that recombinant *Mt*UvrA was purified in the absence of any intentional external source of DNA damage, we speculate that the exposure of the sample to a pro-oxidative environment resulting from cell lysis, and/or the prolonged binding to a nickel-based matrix, could have induced oxidation of *E. coli* genomic DNA, which then served as the substrate for UvrA[28], overall explaining the abundance of the *Mt*$UvrA_2$-DNA complexes in our sample.

Single-particle cryo-EM analysis of the *Mt*UvrA-*Mt*UvrB-DNA complex reveals three assembly states with a hierarchical reconfiguration

The optimal superposition of *Mt*$UvrA_2$-DNA reconstruction to the *Bst*$UvrA_2$-$UvrB_2$ complex[5] (PDB: 3UWX) revealed that both *Bst*UvrB monomers would collide with the dsDNA molecule present in our model (Supplementary fig. 4a), suggesting that critical structural rearrangements should take place to allow the simultaneous binding of UvrB and dsDNA to *Mt*$UvrA_2$. Therefore, we attempted the long-sought structural characterization of the UvrA-UvrB-DNA complex through the use of a synthetic dsDNA molecule (DNA*) with a 10-nucleotide single-stranded 5' overhang ends with high affinity for UvrB[15] and two internal fluorescein-modified nucleobases separated by four base pairs that mimic bulky lesions recognized by UvrA[19] (Supplementary Table 3, Supplementary fig. 4b).

We assembled and purified the *Mt*UvrA-*Mt*UvrB complex and subsequently mixed it with the DNA*. The sample was vitrified, and cryo-EM data were collected (Supplementary figs. 5, 6 and Supplementary Table 1). Following 3D reconstruction, three kinds of oligomeric assemblies (namely *Mt*$UvrA_2$-DNA, *Mt*$UvrA_2UvrB_1$-DNA and *Mt*$UvrA_2UvrB_2$-DNA) were identified and independently processed to a resolution of 3.2 Å, 4.3 Å and 3.7 Å, respectively (Fig. 2, Supplementary fig. 5 and Supplementary fig. 6a).

The *Mt*$UvrA_2$-DNA reconstruction showed a signal for the dsDNA longer than the one expected for DNA* (Supplementary fig. 7); moreover, the map superposed well (CC = 0.92) with the previously obtained *Mt*$UvrA_2$-DNA map, thus we concluded that it represents the structure of *Mt*$UvrA_2$ associated to the co-purified *E. coli* DNA. Considering the final resolution of the two reconstructions, we decided to focus our analyses on the latter one.

The *Mt*$UvrA_2UvrB_2$-DNA and *Mt*$UvrA_2UvrB_1$-DNA reconstructions exhibited anisotropic behavior due to significant preferential orientation, resulting in a lower map quality than expected for their calculated FSC resolution (Supplementary fig. 6b, c). Nevertheless, the quality of both reconstructions enabled the building of a model through rigid-body fitting of the different domains of UvrA and UvrB (Fig. 2b). Both reconstructions did not exhibit signal for dsDNA since the density is compatible with ssDNA overhangs bound to UvrB, exactly as in DNA* (Supplementary fig. 8). Accordingly, the experimental procedure that we designed allowed us to stabilize two complexes between *Mt*UvrA, *Mt*UvrB and DNA* with two distinct

https://doi.org/10.1038/s41467-025-58670-0

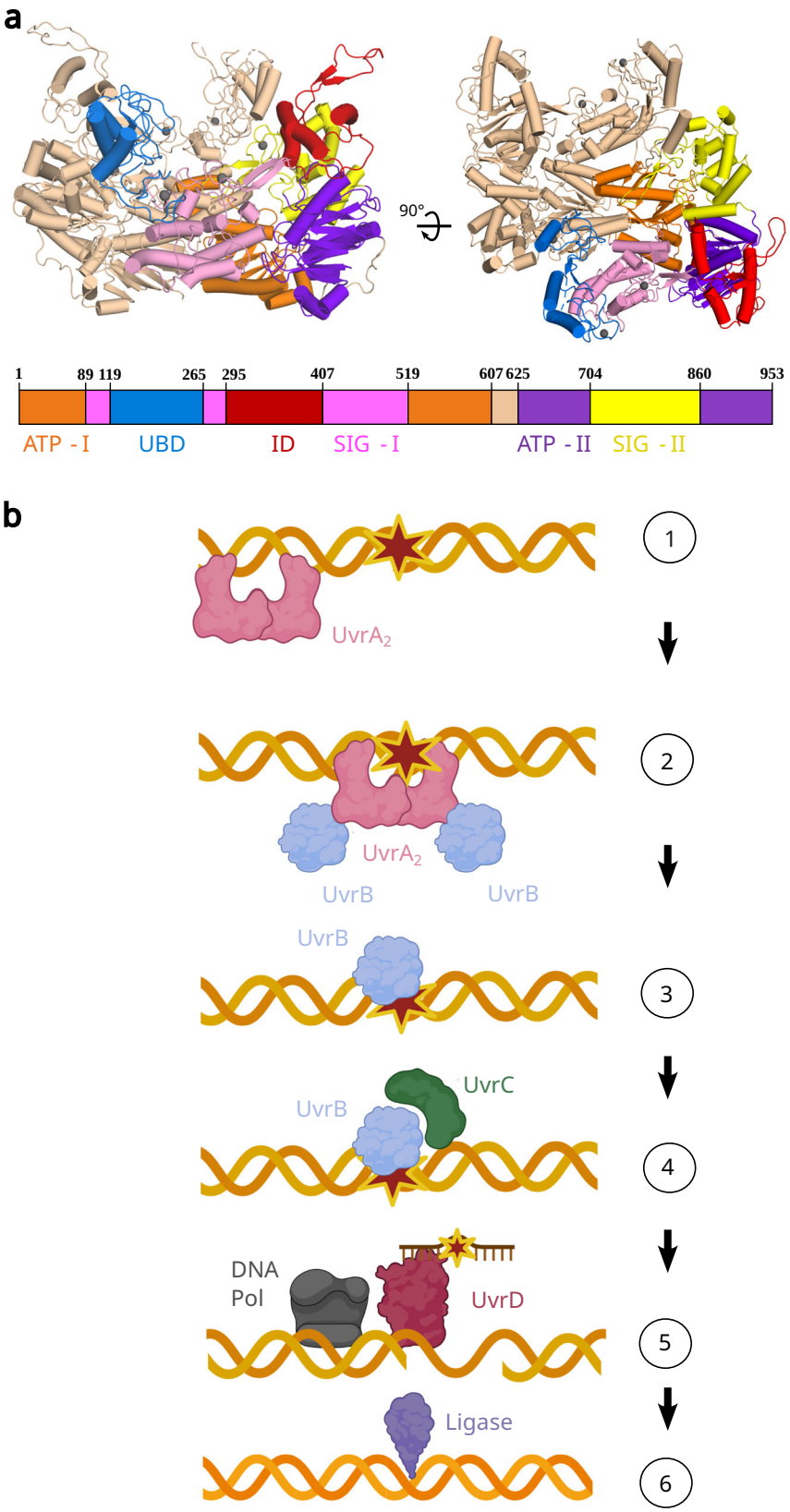

Fig. 1 | Schematic representation of UvrA structure and NER overall pathway. **a** Crystal structure of *Mt*UvrA$_2$ (PDB: 3ZQJ) in two orientations. UvrA domains were colored according to the schematic diagram (the terms ATP-I and ATP-II are used to indicate the proximal and distal ATP binding site, respectively. Similarly, SIG-I and SIG-II are indicative of signature domains, while UBD stands for UvrB binding domain and ID for Insertion Domain). **b** Schematic representation of the different steps of prokaryotic NER: damage search process (lesion is depicted with a red star) performed by either UvrA$_2$ or UvrA-UvrB complex (1); damage identification and consequent recruitment of UvrB molecules (2); pre-incision complex formation and UvrA detachment (3); UvrC recruitment and damaged DNA incision (4); restoration of the native dsDNA, operated by UvrD, DNA Polymerase I and ligase (5 and 6). Created in BioRender. Ferraris, D. (2024) BioRender.com/f96q610.

https://doi.org/10.1038/s41467-025-58670-0

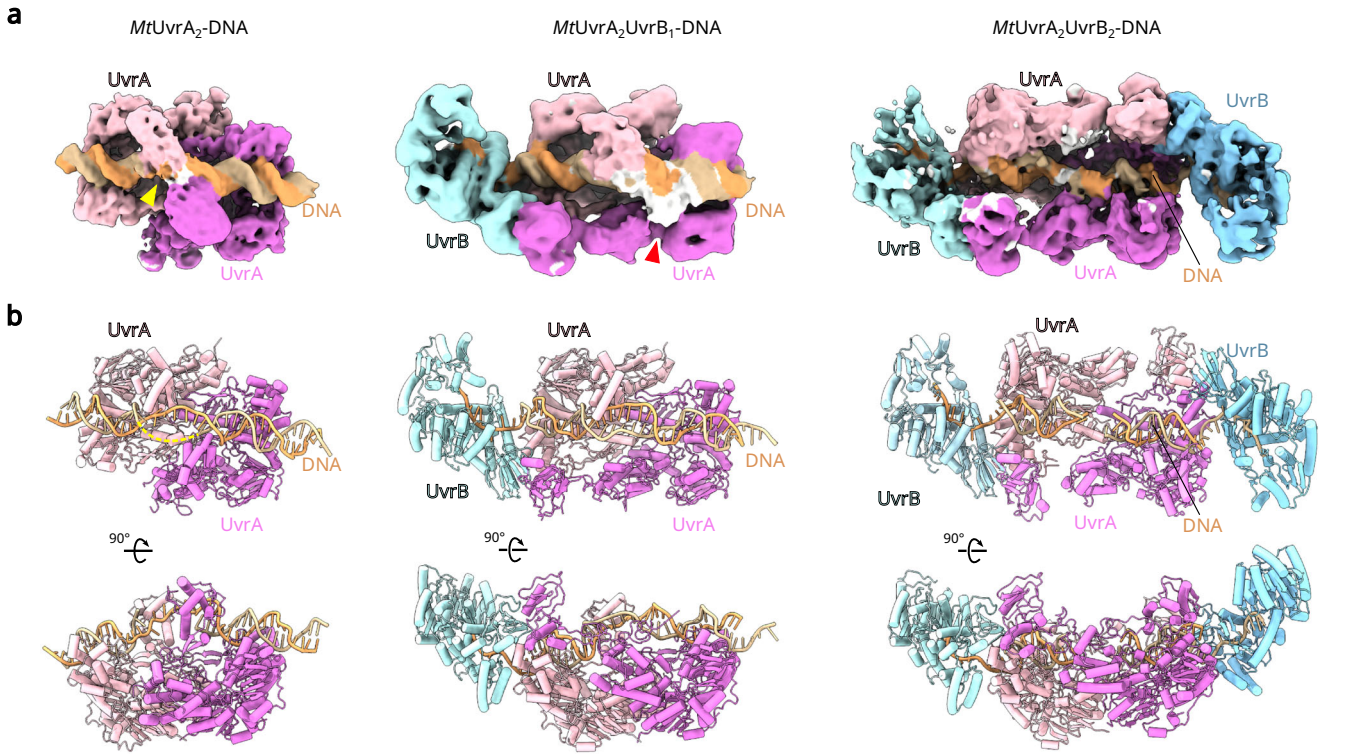

Fig. 2 | Cryo-EM structures of *Mt*UvrA$_2$-DNA, *Mt*UvrA$_2$UvrB$_1$-DNA* and *Mt*UvrA$_2$UvrB$_2$-DNA* complexes. a The indicated cryo-EM reconstructions are color coded and labeled according to the models shown in **b**; in the *Mt*UvrA$_2$-DNA and *Mt*UvrA$_2$UvrB$_1$-DNA* reconstructions, the yellow and the red arrowhead points out the lack of signal corresponding to a 7-nt long segment of one DNA strand, and to one *Mt*UvrA protomer ID, respectively. **b** Cartoon representation of the *Mt*UvrA$_2$-DNA, *Mt*UvrA$_2$UvrB$_1$-DNA* and *Mt*UvrA$_2$UvrB$_2$-DNA* models in two orientations; in the side views it is possible to appreciate the initial bending of the DNA in *Mt*UvrA$_2$-DNA and *Mt*UvrA$_2$UvrB$_1$-DNA* and the final position in the groove of *Mt*UvrA$_2$UvrB$_2$-DNA* structure. The unmodeled DNA strand segment on *Mt*UvrA$_2$-DNA is represented with a dashed line.

stoichiometries, which, in conjunction with the *Mt*UvrA$_2$-DNA, represent three structures of macromolecular assemblies acting in the initial stages of mycobacterial NER.

Remarkably, in the three different protein-DNA complexes it is possible to distinguish two different DNA configurations: indeed, although the central DNA portion in *Mt*UvrA$_2$-DNA is characterized by lower resolution (Supplementary fig. 6b), it is evident that the oligonucleotide is bent (~ 28°) and locally melted, as in *Mt*UvrA$_2$UvrB$_1$-DNA* complex, while the DNA in *Mt*UvrA$_2$UvrB$_2$-DNA* complex has been observed in a linear configuration, lying in the groove of UvrA dimer with the same positioning of *Tm*UvrA$_2$-DNA[7] (Fig. 2b). In all the complexes, the protein-DNA interactions result in a local alteration of the base pair parameters, among which rise and twist angle values diverge from the expected patterns for a canonical B-DNA structure[29–31].

The *Mt*UvrA IDs play a central role in DNA unwinding, melting and the flipping of a nucleobase into a potential lesion recognition state

The structure of *Mt*UvrA$_2$-DNA shows the same organization of the core catalytic domains observed in the crystallographic structure of the *Tm*UvrA$_2$-DNA (PDB: 3PIH)[7], with slight changes in the Signature-I and the C-terminal Zn-finger β-hairpins$_{761\text{-}775}$ (Supplementary fig. 9a, b). Still, the C-terminal Zn-finger β-hairpins$_{761\text{-}775}$ adopt the same open conformation that was suggested to be correlated to DNA binding. Protein-DNA contacts along the Signature-II domain are mostly conserved, with a minor variation between the loop$_{704\text{-}709}$ and the phosphate backbone due to the deformation of the DNA (Supplementary fig. 9c). A striking difference is observable at the level of the IDs: while in the *Tm*UvrA$_2$-DNA structure they do not contact the DNA molecule, in our *Mt*UvrA$_2$-DNA reconstruction they clamp both sides of the flat segment in the middle of the DNA double helix, which displays a 28° bending and different degrees of unwinding: when compared to the canonical B-DNA, the flat central portion of the DNA displays -16° of unwinding and the nucleobases flanking this region (A/T16 and A/T27) 9° of unwinding (calculated with w3DNA 2.0 software[31]). As a result, the major groove-corresponding surface of the unwound dsDNA region faces the catalytic core of the *Mt*UvrA dimer, while the widened minor groove faces upwards (Fig. 3a). Each ID holds in place one of the complementary DNA strands, by using the α-hairpin$_{381\text{-}405}$ and the α-hairpin$_{313\text{-}335}$, with the α-helix$_{320\text{-}335}$ deeply inserted into the DNA minor groove (Fig. 3a and Supplementary fig. 10a).

The path of the DNA sugar-phosphate backbone is a key attribute particularly well-defined in our reconstruction, except for a 7 nucleotide-long region that contacts one of the two IDs (Figs. 2 and 3a). The poor signal may indicate DNA flexibility, as a probable result of the base-pairing loss due to the presence of the damage; this base-pairing loss as well as base-stacking alteration in the vicinity of the lesion could be the hallmark that UvrA senses to recognize the presence of the damage site. A more detailed analysis of the ID-DNA interface, complementary to the disordered strand, revealed a notable signal oriented backward with respect to the position of the nucleobases (Supplementary fig. 10b). The better definition of the DNA reconstruction with respect to the ID part, together with the fact that nucleobases scatter electrons particularly well, lead us to interpret this signal as a flipped-out nucleobase (Fig. 3b). Interestingly, the reoriented nucleobase is hosted in a hydrophobic pocket within the ID, adopting an overall conformation that matches well the one observed in the structure of UvrB-DNA complex, in which an extruded cytosine occupies an equivalent hydrophobic pocket between domains 1a and

https://doi.org/10.1038/s41467-025-58670-0

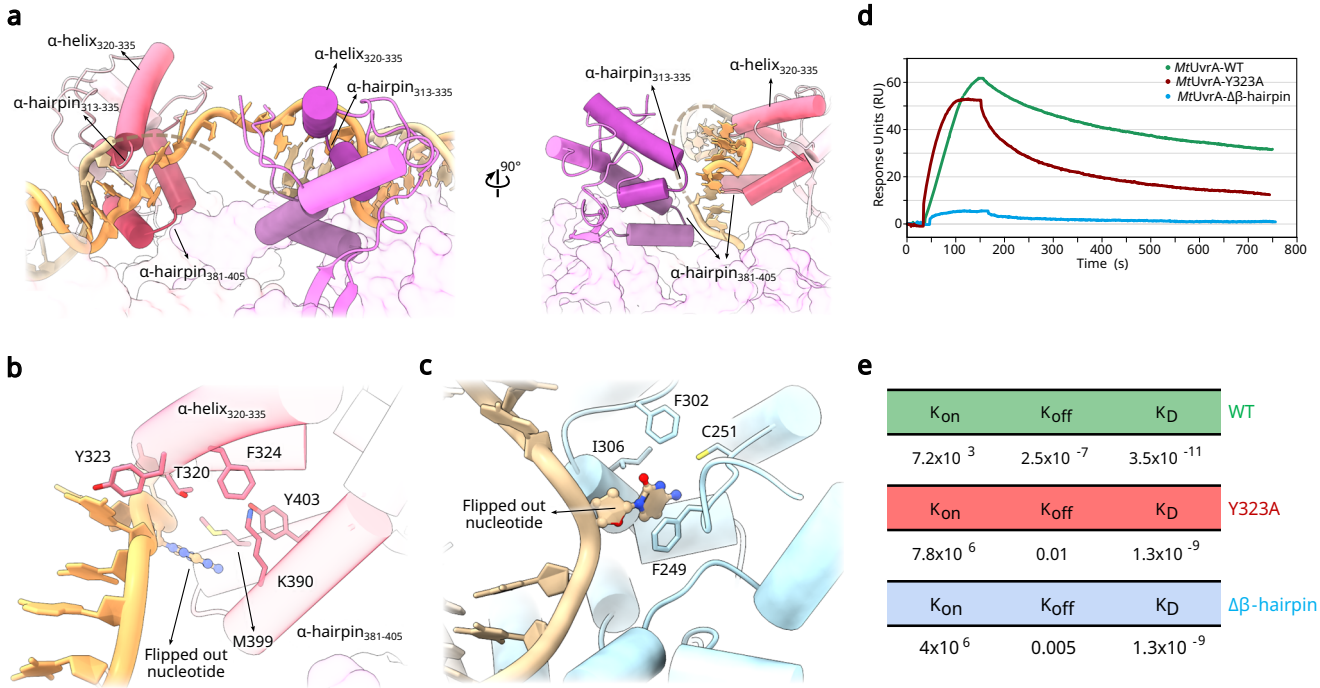

Fig. 3 | Roles of *Mt*UvrA IDs in DNA clamping and characterization of the damaged-dsDNA binding activity of the wild type enzyme and mutated variants. a Closeup of the *Mt*UvrA dimer IDs, showing the structural motifs/elements that are engaged in clamping and deforming the DNA molecule (in orange); in both panels, the region of one DNA strand that is not defined in the model is represented by a dashed line and β-hairpins$_{363\text{-}377}$ were not modeled. **b** Detailed view of the flipped-out nucleotide; functionally relevant residues of the recognition-ID hydrophobic pocket are displayed as sticks and labeled, as well as Tyr323. **c** Flipped-out nucleotide in UvrB-DNA complex (PDB: 6O8F)[12], accommodating into the hydrophobic pocket between domains 1a and 1b. **d** SPR sensorgrams of MtUvrA proteins (wild type and mutated variants) binding to the damaged-DNA probe immobilized on a sensor chip. **e** Calculated K_{on}, K_{off} and K_D values are shown for each investigated variant. Source data are provided as a Source Data file.

1b[12] (Fig. 3c). It is noteworthy that the side-chain of the tyrosine residue at position 323 of the α-helix$_{320\text{-}335}$ (Y323) appears properly positioned to potentially replace the missing flipped-out base within the DNA π-stacking. As a matter of fact, sequence alignment showed that the Y323 residue is highly conserved among UvrA of different species (Supplementary fig. 11), supporting a key role in the clamping.

A disordered DNA strand and an extruded nucleobase are structural hallmarks found in other helicases[32–34] and in the lesion recognition process of other DNA repair enzymes[35–37]. Notably, in our structure these two features are exclusively observable at the level of the ID that is engaged in a potential damage recognition conformation, indicating a division of labor between the two IDs. Consequently, we will refer to the ID that hosts the flipped nucleobase as the "recognition-ID", and we will indicate the other one as the "support-ID" (Supplementary fig. 10a).

The inspection of *Mt*UvrA$_2$-DNA reconstruction revealed a continuous extra density above the minor groove corresponding to the flat face of the dsDNA; the signal is large enough to host the two unmodeled ID β-hairpins$_{363\text{-}377}$ (Supplementary fig. 10c), which, in this position, would directly contact the DNA. In general, β-hairpins are conserved motifs in helicases involved in DNA melting[24]. The *Mt*UvrA ID β-hairpin$_{363\text{-}377}$ is particularly enriched with conserved arginine and tyrosine residues (Supplementary fig. 11), that have the potential to interact with DNA sugar-phosphate backbone and to establish π-stacking contacts with nucleobases, thereby interfering with base pairing. Considering the conformation and the amino acid composition of the *Mt*UvrA ID β-hairpin$_{363\text{-}377}$, we propose that it could play a prominent role in DNA melting. A sequence comparison analysis highlighted a high degree of conservation of this element among species, except for the hyperthermophiles *Thermotoga maritima* and *Aquifex aeolicus*. In such cases, the high temperatures of the ecological niche of these organisms may facilitate spontaneous dsDNA local melting, even in the absence of a β-hairpin, equivalent to the *Mt*UvrA ID β-hairpin$_{363\text{-}377}$ (Supplementary fig. 11).

Although previous works highlighted the role of IDs in stabilizing the complex with damaged DNA through DNA locking and melting[8], to date there is no structural model describing the molecular details of this phenomena[38,39]. Although we were unable to unambiguously establish the identity of the dsDNA component fortuitously captured in the *Mt*UvrA$_2$-DNA complex, the overall molecular architecture revealed by our cryo-EM structure is consistent with a genuine lesion recognition state. To verify the hypothesized contribution of the ID β-hairpin$_{363\text{-}377}$ and Y323 to the *Mt*UvrA lesion-sensing function, we challenged the damaged-DNA binding activity of two protein variants: *Mt*UvrA-Δβ-hairpin, lacking the entire ID β-hairpin$_{363\text{-}377}$, and *Mt*UvrA-Y323A, in which Y323 is substituted by an alanine. We performed two pilot experiments (Electrophoretic Mobility Shift Assay - EMSA - and Microscale Thermophoresis - MST) using a DNA fragment with the same nucleotide sequence as DNA*, containing 2 fluorescein-dT (FLUdT) mimicking a bulky nucleobase adducts (probe) (Supplementary Table 3); these analyses indicated that the damaged-DNA binding activity of the two variants is severely compromised, compared to the one of wild type *Mt*UvrA (Supplementary fig. 12 a,b). To obtain further detailed information, we characterized the binding of *Mt*UvrA and mutated variants with the damaged DNA with surface plasmon resonance (SPR): the use of a sensor chip functionalized with the same probe revealed that not only *Mt*UvrA, but also its two protein variants can bind damaged-DNA, although displaying different kinetics (Fig. 3d). In particular, UvrA-Δβ-hairpin and UvrA-Y323A mutants displayed a dissociation phase sensibly faster than those characterizing the wild-type protein (Fig. 3e), which explains why with non-real-time assays (EMSA, MST) we detected no binding: the dissociation of the mutants is too fast, leading to a non-stabel interactions with the damaged DNA. Furthermore, the binding of the *Mt*UvrA variants to the

https://doi.org/10.1038/s41467-025-58670-0

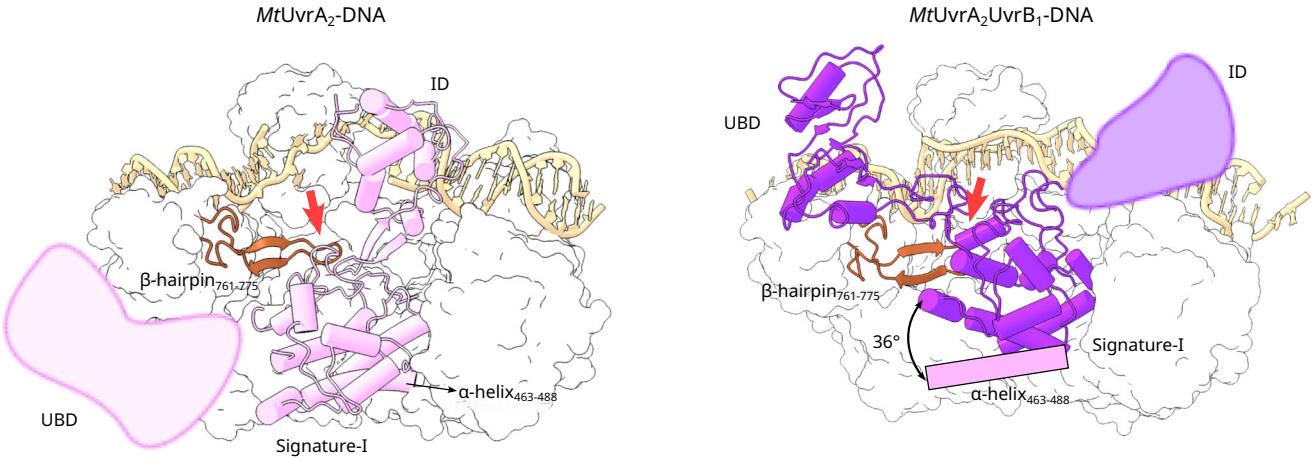

Fig. 4 | *Mt*UvrA conformational switch upon *Mt*UvrB binding. Composite graphical representation of *Mt*UvrA$_2$-DNA (left) and *Mt*UvrA$_2$UvrB$_1$-DNA* (right) structures. In both panels, the *Mt*UvrA domains that undergo a substantial repositioning upon *Mt*UvrB binding (ID, UBD, Signature-I and the β-hairpin$_{761\text{-}775}$) and the DNA are represented as cartoon. The missing domains in each structure (UBD in *Mt*UvrA$_2$-DNA and ID in *Mt*UvrA$_2$UvrB$_1$-DNA*) are represented as plane-colored shapes. The curved arrow in the panel on the right indicates the approx. 40 ° rotation of the Signature-I domain (as evaluated by comparing the position of the α-helix$_{463\text{-}488}$ in the two models). In each image, the red arrow points to the contacts established between either the Zn-module (left) or the Signature-I domain (right) of one *Mt*UvrA protomer and the C-terminal Zn finger β-hairpin$_{761\text{-}775}$ of the opposite one in the dimer. For clarity, the UvrB molecule has been omitted.

DNA ligand resulted in a lower response, as evidenced by the reduced resonance units count (Fig. 3d). Therefore, the biochemical data support our structural observations, indicating that the β-hairpin$_{363\text{-}377}$ and Y323 represent crucial elements for binding damaged DNA by increasing the retention time on the lesion.

Overall, the collective evidence lends support to a model in which the *Mt*UvrA$_2$-DNA structure represents a state wherein UvrA clamps, unwinds and melts dsDNA through the IDs. The recognition-ID is responsible for nucleobase flipping, while β-hairpin$_{363\text{-}377}$ may facilitate melting by interacting with the minor groove face of the DNA. We suggest that this model represents the end point of the UvrA-promoted lesion recognition process.

Concerning the ATP/ADP binding state, we are able to observe the presence of ADP in the distal sites of the dimer (Supplementary Fig. 13), while the proximal sites are empty. This agrees with previous observations that suggest that UvrA dimer is often more stable in the presence of a mixed nucleotide-bound/free species, in which the proximal site is empty and the distal site may be occupied by ATP or ADP[19,22,40]. In addition, this correlates well with what observed and proposed previously[41]: the genome scanning activity and the discrimination between native and damaged DNA require ATP hydrolysis at the distal sites, which are demonstrated to consume ATP in a fast way, releasing phosphate; the proximal sites, instead, have been implicated in interactions between UvrA and UvrB, playing an important role in recruiting UvrB to the damaged site[40,42]. In our model, we are able to see ADP molecules fulfilling the distal sites, supporting the idea that *Mt*UvrA$_2$-DNA structure describes the moment in which UvrA recognizes the lesion, while the proximal sites are empty, coherently with the fact that no UvrB molecule is present.

The binding of one *Mt*UvrB molecule to one *Mt*UvrA protomer triggers the concomitant repositioning of the support-ID with consequent DNA release

The cryo-EM *Mt*UvrA$_2$-DNA structure provides a molecular snapshot of an early stage in the NER pathway, in which *Mt*UvrA stably binds a potentially damaged DNA. To investigate the structural changes required for the pathway to proceed, we focused on the *Mt*UvrA$_2$UvrB$_1$-DNA* cryo-EM structure that gave us the opportunity to evaluate the impact of the binding of one UvrB molecule on the overall architecture of the protein-DNA complex.

The reconstruction revealed a loss of signal for the ID belonging to the *Mt*UvrB-bound *Mt*UvrA protomer (Fig. 2a), suggesting that *Mt*UvrB destabilized the *Mt*UvrA ID conformation. The Signature-I domain of the catalytic core of the same *Mt*UvrA protomer underwent a significant repositioning with respect to *Mt*UvrA$_2$-DNA structure (Fig. 4) subsequent to the C-terminal Zn-finger β-hairpins$_{761\text{-}775}$ repositioning, adopting a conformation that closely resemble the one observed in *Bst*UvrA$_2$UvrB$_2$ structure, the only available structure of UvrA in complex with UvrB[5]. The Signature-I domain is connected to both the ID and UBD and properly positions the UBD for UvrB binding. The structural arrangement of the UBD upon *Mt*UvrB binding and the *Mt*UvrA ID-DNA interaction appear mutually exclusive, due to steric hindrance, and consequently ID undergoes a conformational change releasing the DNA (Fig. 4 and Supplementary Movie 1). Moreover, the binding of *Mt*UvrB affects the nearby C-terminal Zn-finger β-hairpin$_{761\text{-}775}$ of the adjacent UvrA protomer that switches from the ID in the *Mt*UvrA$_2$-DNA structure to the Signature-I domain in the *Mt*UvrA$_2$UvrB$_1$-DNA* complex (Fig. 4 and Supplementary Movie 1). This observation led us to propose that the C-terminal Zn-finger β-hairpin$_{761\text{-}775}$ functions as a scaffolding element, alternatively supporting the Signature-I domain or the ID, along the structural rearrangements that are functional to the protein-DNA complexes remodeling.

The hydrophobic pocket of the *Mt*UvrA recognition-ID hosts the lesion independently of UvrB

Despite the lower resolution of the *Mt*UvrA$_2$UvrB$_1$-DNA* cryo-EM map, we could clearly discern the junction between the single-stranded and the double stranded segments (Fig. 5a and Supplementary fig. 8). This permitted the assignment of the nucleotide sequence of our DNA*. One of the lesion-mimicking fluorescein-modified thymine (FLUdT) of DNA* aligned with the recognition-ID, that is still defined in our structure (Fig. 5b). This evidence suggests that the first *Mt*UvrB binding event induces the release of the support-ID only, while the recognition-ID remains stably associated to the lesioned-strand via the clamping α-hairpins. Moreover, in the *Mt*UvrA$_2$-DNA complex, the flipped-out nucleotide binds at the hydrophobic pocket of the recognition-ID by adopting a pose that perfectly matches the one displayed by the genuine modified-nucleobase (i.e. FLUdT) in the *Mt*UvrA$_2$UvrB$_1$-DNA* complex (Fig. 5b).

The capacity of the recombinant *Mt*UvrA to bind and copurify with endogenous *E. coli* oxidized DNA, the low dissociation rate showed through SPR data and the extensive interactions shown in the *Mt*UvrA$_2$-DNA structure underpin that *Mt*UvrA is able to lock the lesioned-DNA in a highly stable complex as previously described[13,16].

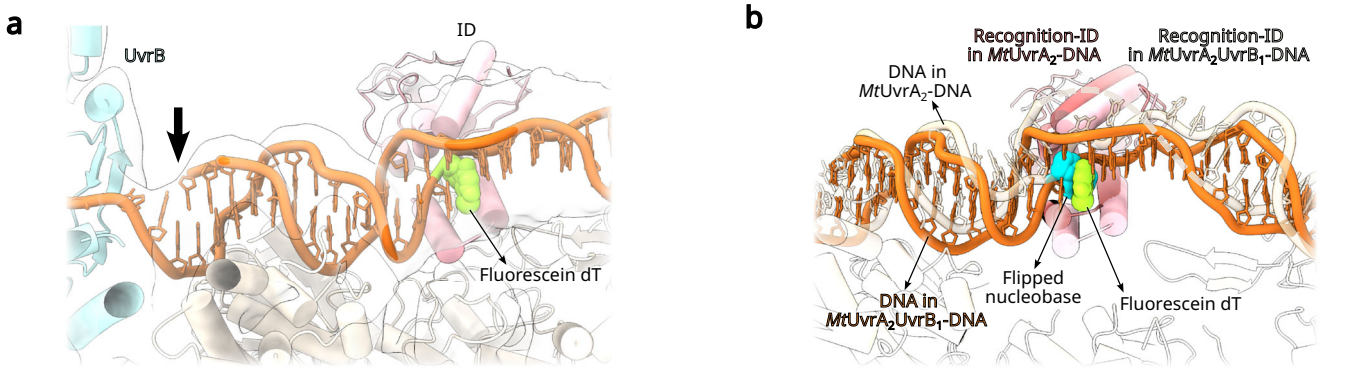

Fig. 5 | Detailed views of the DNA lesion within the *Mt*UvrA recognition-ID. **a** Cartoon representation of the *Mt*$UvrA_2UvrB_1$-DNA* with the fluorescein dT highlighted as green spheres. The cryo-EM reconstruction is shown as semi-transparent surface. The unpaired-to-paired DNA transition was marked with an arrow. **b** Superposition of *Mt*$UvrA_2UvrB_1$-DNA* and *Mt*$UvrA_2$-DNA structures. The fluorescein dT, the DNA and the recognition-ID in *Mt*$UvrA_2UvrB_1$-DNA* appear in green, orange and pink, respectively. The flipped-out nucleobase, the DNA and the recognition-ID in *Mt*$UvrA_2$-DNA are colored in cyan, white and red, respectively. The missing segment of one DNA strand in *Mt*$UvrA_2$-DNA structure is represented with a dashed line.

On the other hand, in *Mt*$UvrA_2UvrB_1$-DNA* reconstruction, we observed the release of one ID (support-ID) with the concomitant binding of one UvrB molecule to the same UvrA protomer. This poses the question on how UvrB recognizes the UBD associated to the support-ID; we speculate that the driving force for the first UvrB binding event relies on a thermodynamic principle: it is likely that the binding energy of each ID is different, because of the presence of the lesion on one side of the DNA; the binding affinity of the recognition-ID is expected to be higher than one of the support-ID. This results in a low free-energy gain during the release of the support-ID and therefore the binding, with the associated conformational changes, is favored in the support-ID-containing UvrA protomer. The absence of a signal for *Mt*UvrB or the UBD in the *Mt*$UvrA_2$-DNA reconstruction suggests that *Mt*UvrB is dispensable to reach such a "locked-in-damage" stage. Moreover, the *Mt*$UvrA_2UvrB_1$-DNA* points out that *Mt*UvrB triggers a dramatic structural remodeling of the IDs in *Mt*$UvrA_2$-DNA complex. Our findings support previous works that established that UvrA is responsible for the first damage identification event, exhibiting discrimination between damaged and undamaged DNA based on the residence time on the DNA, subsequently addressing UvrB to the lesion[16,40].

The binding of two UvrB molecules destabilizes the UvrA dimer interface and set the ground for the lesion hand-off between UvrA and UvrB

The overall "Venetian gondola" assembly of *Mt*$UvrA_2UvrB_2$-DNA* resembled the one observed in the *Bst*$UvrA_2UvrB_2$ structure (PDB: 3UWX)[5]. In both models, each UvrB interacts with a UBD and a Signature-II domain of opposite protomers (Fig. 2b). Both structures exhibited the same conformation for the catalytic core, including the interplay between the Signature-I domain and the C-terminal Zn-finger β-hairpin$_{761\text{-}775}$, as observed in the *Mt*$UvrA_2UvrB_1$-DNA* complex. Additionally, the disengagement of both IDs makes the DNA* free to position inside the *Mt*$UvrA_2$ central groove; the resolution in the central region of the DNA is very low, which is probably caused by the DNA being disordered in this part: indeed, we decided not to model it; nevertheless, a B-DNA cannot fit in the density in that region.

This conformation in which both IDs are open and two UvrB molecules are bound further confirms the association between *Mt*UvrB binding and ID displacement.

A remarkable similarity between *Mt*$UvrA_2UvrB_2$-DNA* and *Bst*$UvrA_2UvrB_2$ structures is that the IDs share a similar orientation (Fig. 6a). In both cases, each ID opens wide to approach the ATP-binding domain II. Nevertheless, in *Bst*$UvrA_2UvrB_2$ structure the ID repositioning is less pronounced, as a possible consequence of the interactions established between the symmetry mates in the crystal lattice. Given that the same structural configuration was observed in the presence as well as in the absence of DNA, we postulate that UvrB binding not only displaces the IDs, but it also drives the proper IDs repositioning towards the ATP-binding domains II.

Remarkably, the structural rearrangement induced by *Mt*UvrB brings each ID at a 26 Å distance to the *Mt*UvrB molecule bound to the opposite *Mt*UvrA protomer (Fig. 6a). Given that the recognition-ID represents the primary damage recognition element in *Mt*UvrA and that the support-ID disengages DNA upon the first *Mt*UvrB binding event, we are tempted to speculate that the recognition-ID repositioning could move the lesion in close proximity to the already bound *Mt*UvrB (Fig. 6b). Although this hypothesis would require further demonstration, the proposed mechanism satisfies four important requirements for the formation of the pre-incision complex: i) the UvrB β-hairpin inserts through the DNA major groove[43,44], whereas the recognition-ID of UvrA interacts with DNA through the minor groove; therefore, the repositioning of the recognition-ID, together with the lesion held in place, would make the major groove accessible for the insertion of UvrB β-hairpin. ii) The damaged nucleobase recognized by the recognition-ID locates in the 3′-to-5′ DNA strand; consequently, the recognition-ID holds the lesion and repositions towards a pre-bound UvrB, which is capable of 5′-3′-directed translocation[45]. iii) The melted DNA region matches the proposed 6nt-long bubble necessary for UvrB interaction[23]. Finally, iv) the flipped-out lesion in UvrA agrees with the proposed UvrB lesion recognition mechanism through a base extruded from the DNA helix[12,14].

In our cryo-EM single particle analysis of *Mt*$UvrA_2UvrB_2$-DNA*, we detect flexibility between two halves. Each half contains one *Mt*UvrB molecule, a DNA fragment and all domains within one *Mt*UvrA protomer except for the UBD that belongs to the second protomer (Supplementary fig. 5). So, the *Mt*$UvrA_2UvrB_2$-DNA* complex is flexible and behaves as two rigid body halves that hinge through the *Mt*UvrA dimerization interface. This is an unprecedented characteristic with respect to previous UvrA structures that showed an extensive interaction between UvrA protomers of 2849 Å^2. In contrast, in *Mt*$UvrA_2UvrB_2$-DNA* the UvrA dimer interface is 1189 Å^2, a decrease of 60% (Supplementary Table 4). Moreover, this observation agrees with the *Bst*$UvrA_2UvrB_2$ structure, which shows a comparable decrease. Therefore, both structures align with the idea that the structural rearrangement produced by the second UvrB molecule binding triggers UvrA interprotomer destabilization; analyzing these three structures in succession (*Mt*$UvrA_2$-DNA, *Mt*$UvrA_2UvrB_1$-DNA* and *Mt*$UvrA_2UvrB_2$-DNA*), it is possible to observe that the binding of

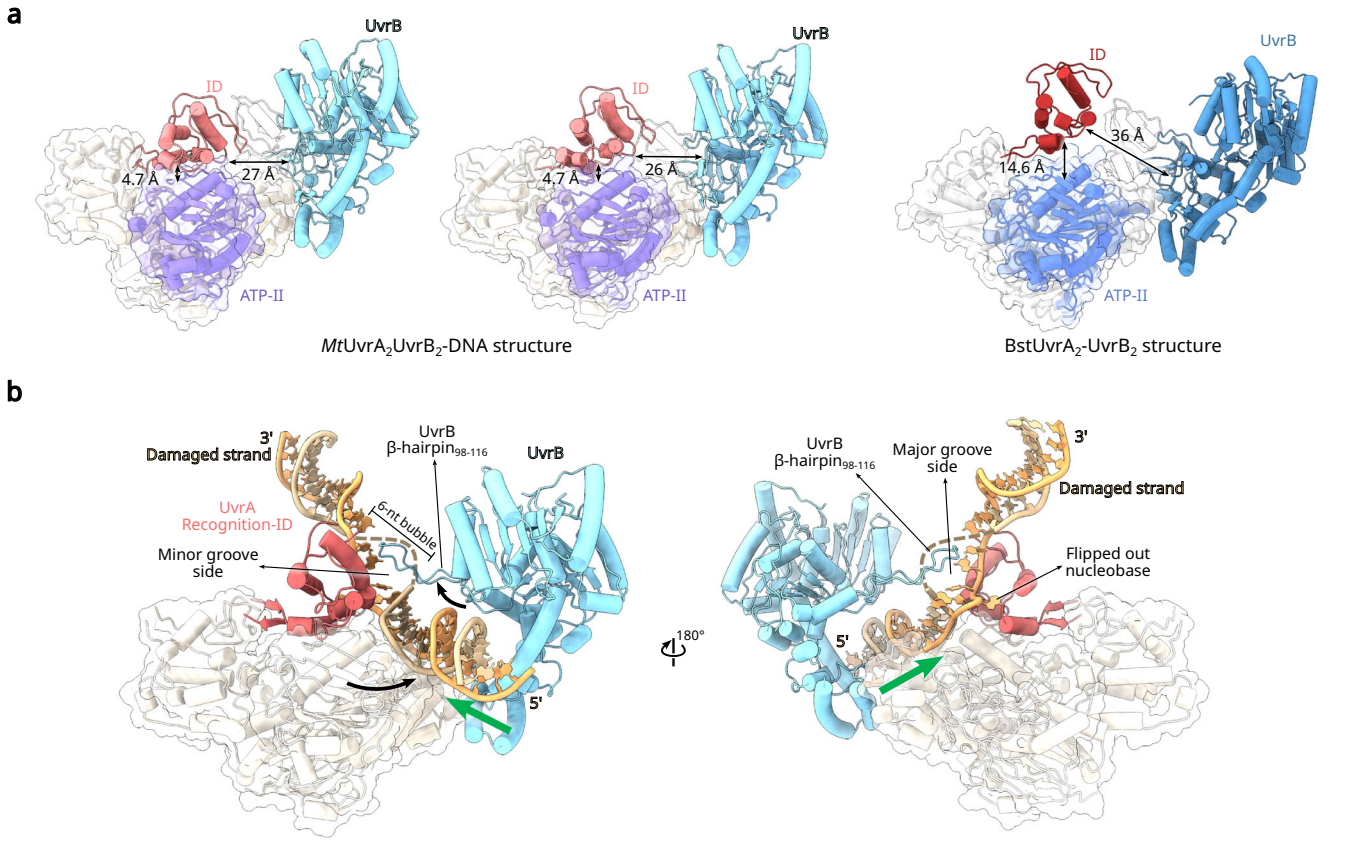

Fig. 6 | UvrA ID repositioning over the ATP-binding domain II and close to UvrB could promote the transfer of the lesion from UvrA to UvrB. a The image on the left represents the models of both the UvrA-UvrB heterodimers observed in the *Mt*UvrA$_2$UvrB$_2$-DNA* structure; the UBDs were not represented for a better visualization. The image on the right corresponds to an equivalent heterodimeric component within the *Bst*UvrA$_2$UvrB$_2$ structure. The ID, the ATP-binding domain II (ATP-II) and UvrB are differently colored and labeled. The distances between ID and ATP-II, and the tip of α-hairpin$_{381\text{-}405}$ and Asn117 of UvrB (Ans116 in *Bst*UvrB) are indicated as double arrows. **b** Structure-based hypothetical model for the lesion hand-off (two 180° rotated images are shown). Upon optimal superposition, the ID of *Mt*UvrA$_2$UvrB$_2$-DNA* structure was superposed and replaced with the ID and the DNA of *Mt*UvrA$_2$-DNA structure; the DNA and the UvrB β-hairpin$_{98\text{-}116}$ were shifted to avoid clashes and marked with black arrows. Important elements in the model are highlighted and labeled. The missing region in one DNA strand is represented with a dashed line. The green arrow indicates the direction of the short-range translocation of UvrB on the DNA.

the DNA in *Mt*UvrA$_2$-DNA triggers the opening of the C-terminal Zn-finger β-hairpins$_{761\text{-}775}$ with respect to *Mt*UvrA$_2$, which causes the repositioning of the SIG-1 domain, leading to the opening of the ID and to the binding of UvrB on the same protomer that exposed the ID; the same events happen for the other protomer, leading to the configuration of *Mt*UvrA$_2$UvrB$_2$-DNA*, in which the dimerization interface is destabilized. It is plausible, therefore, that the destabilization event is caused by a series of conformational changes, triggered by the damage recognition. Since UvrA requires dimerization to bind DNA[46], the UvrA dimer destabilization and potential disassembling could culminate in DNA release. DNA release from UvrA is strictly required during the lesion hand-off to UvrB. Therefore, these two key features of *Mt*UvrA$_2$UvrB$_2$-DNA* structure (ID repositioning and UvrA dimer disassembly) support a model in which the recognition-ID repositions to transfer the damage to UvrB.

Discussion

The structures and biochemical analysis presented here elucidate some of the unanswered questions regarding the damage detection mechanism of UvrA and the transfer of the lesion to UvrB. In particular, we observe three conformations that we interpret as representative of sequential events in the initial stages of NER. This observation leads us to propose a model regarding the process that bridges the damage recognition by UvrA and the formation of the pre-incision complex. As showed in Fig. 7, UvrA first dimerizes to properly bind DNA[7] (Fig. 7, step 1 and 2); then, unknown conformational changes, probably triggered by ATP/ADP binding and hydrolysis, lead to UvrA in a locked-in-damage state represented by our *Mt*UvrA$_2$-DNA structure (Fig. 7, step 3), in which it clamps, bends and unwinds DNA through the IDs. In this context, several experimental evidences show that DNA bending and melting is functional for the NER pathway for a proper incision operation[47–49]. Moreover, it has been proposed that UvrA, also independently of UvrB, is able to induce a slight bending of DNA that gradually becomes more severe along the pathway to a point of DNA kinking and wrapping in the pre-incision complex[49–51]. Our observations are in good agreement with single-molecule studies; indeed, Stracy et al. recorded two different modes of UvrA's interactions with DNA during its searching for lesions[16]: a slowly moving state in which UvrA makes transient interaction with the DNA ($<<15$ ms) and a more stably bound state. The authors concluded that these long DNA-bound state represents the damage verification process in which UvrA takes time to sample DNA conformations to verify the presence of a lesion. In this sense we can suggest that what we observed in our *Mt*UvrA$_2$-DNA model is not related to the transient binding mechanism while it can be associated to the verification step, the long-bound state, in which UvrA tests the presence of the lesions through conformational changes leading to active distortions of the DNA molecule. Subsequently to the damage recognition, the binding of the first UvrB molecule displaces the support-ID releasing one DNA strand (Fig. 7, step 4 and Supplementary Movie 2). However, in the *Mt*UvrA$_2$UvrB$_1$-DNA*

https://doi.org/10.1038/s41467-025-58670-0

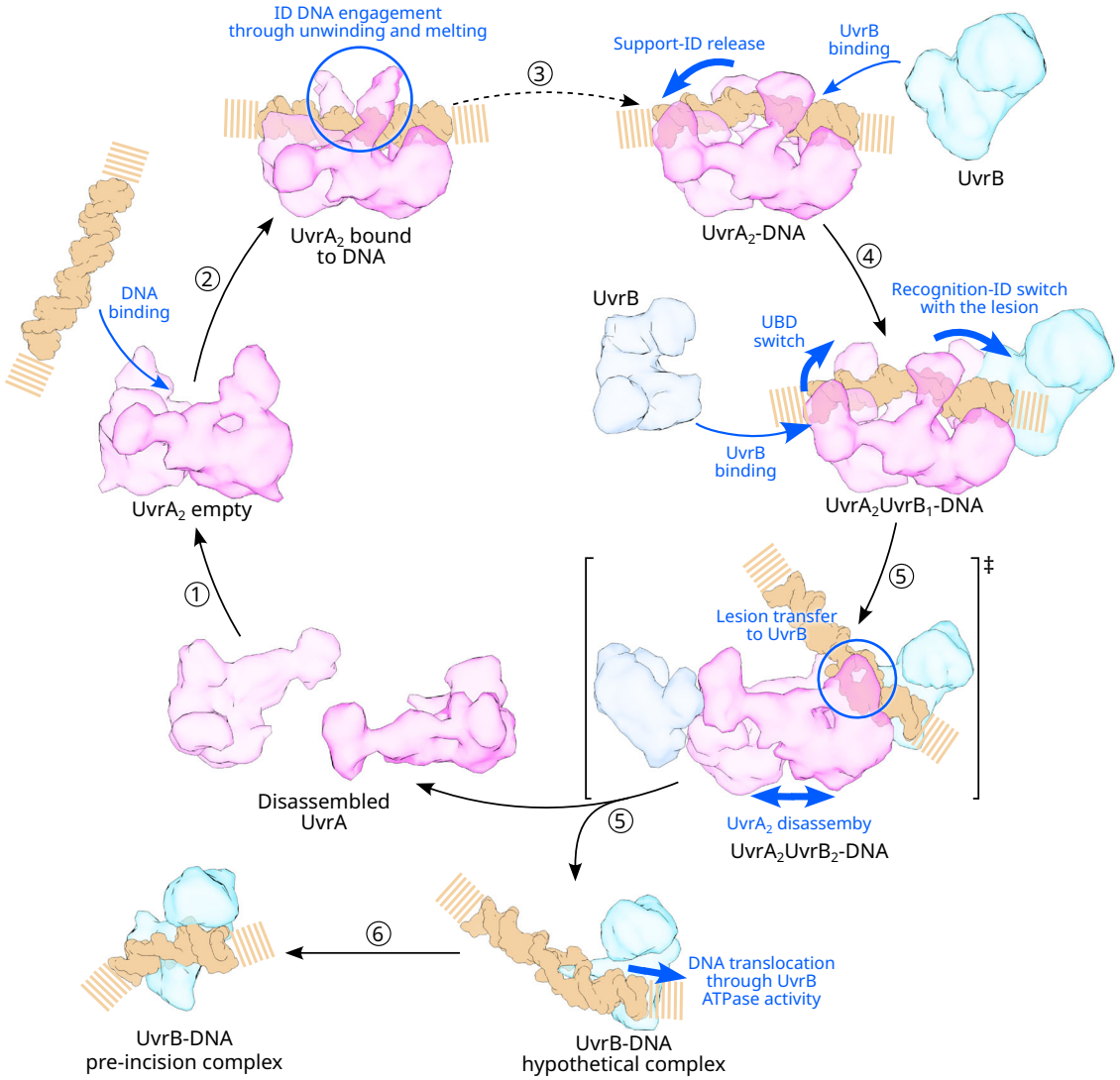

Fig. 7 | Model for the molecular events bridging the damage identification operated by UvrA-UvrB and pre-incision complex formation. UvrA dimerizes (1) to bind DNA (2); the damaged DNA recognition event triggers unknown conformational changes, leading to the bending, unwinding and melting of the DNA (3), allowing it to assess the presence of the lesion. After damage identification, one UvrB molecule binds and displaces the support-ID, releasing one DNA strand (4); a second UvrB molecule binds, causing the repositioning of the recognition-ID, which holds the DNA and transfers it towards UvrB (5), together with the UvrA dimer disassembly. This conformational state represents a transition state, that allows UvrB to access the lesion bubble and to replace UvrA (5). UvrB translocates the DNA through its ATPase activity to the pre-incision complex final conformation (6). The main events leading to the following conformation were indicated in blue.

reconstruction, UvrB binds a ssDNA, which deviates from the natural situation where the dsDNA is expected to be present. In such a position, UvrB would clash with an unprocessed dsDNA (Supplementary fig. 4), while it does not when we modeled UvrB as observed in the 6O8E pdb, namely in complex with a bent, unwound DNA showing a flipped-out nucleotide (Supplementary fig. 8). The second UvrB binding event seems to lead to UvrA dimer disassembly, while the recognition-ID repositioning could facilitate UvrB binding to the bubble around the lesion (Fig. 7, step 5 and Supplementary Movie 2). The decreased stability of the UvrA dimer and the ID displacement potentially preparing the lesion hand-off are consistent with the previously reported disassembly of UvrA during the lesion transfer to UvrB[25]. Therefore, it is plausible that, once primed by the second UvrB binding event, the two phenomena simultaneously occur.

Surprisingly, instead of lesion transfer to *Mt*UvrB and complete *Mt*UvrA disassembling, in our *Mt*UvrA$_2$UvrB$_2$-DNA* structure we observed the DNA* deeply inserted in the central groove of the complex with poor signal for the lesion site and only *Mt*UvrA dimer interface destabilization. In this context, our *Mt*UvrA$_2$UvrB$_2$-DNA* structure represents a transition state in which UvrA is unable to transfer the lesion due to the unnatural overhang ends of the DNA*. Therefore, we are tempted to suggest that the DNA bubble containing the lesion would move towards UvrB, dragged by the IDs. The process culminates the pre-incision complex formation through the short-range UvrB translocation to properly position the damage and ready to recruit UvrC (Fig. 7, step 6). It has to be said that this model is speculative: an alternative model may involve the release of DNA by the IDs of UvrA, after the binding of UvrB; this would allow the DNA to slide towards one of the two UvrB molecules positioned on both ends of the complex.

Interestingly, the damage sensing mechanism described here for UvrA is perfectly in line with the available structures of DNA repair proteins that includes modified bases flipping out, DNA bending and, in some cases, unwinding. Particularly remarkable is the agreement with UV-DDB that participates in pyrimidine dimers (CPD and 6-4PP) recognition in eukaryotic NER. UV-DDB bends DNA by 40° allowing a β-hairpin insertion into the double helix and flipping out the modified bases in a lesion-binding pocket[52]. A second meaningful example is the

functional equivalent, but structurally unrelated, yeast protein Rad4 and its human ortholog XPC. As UV-DDB, Rad4 bends DNA by ~40° and inserts a β-hairpin, but in this case, Rad4 flips out the two bases opposite to the lesion[53,54].

The present results offer a structural model of the first steps in NER pathway from UvrA in a locked-in-damage recognition state to the lesion hand-off to UvrB. However, the mechanistic events leading to such a UvrA conformation and the role of ATP hydrolysis remained unanswered. Another important missing piece of information is represented by the description of the molecular bases of the capability of UvrA to discriminate between damaged and undamaged DNA, since an experimental model of UvrA bound to unmodified dsDNA is still lacking.

Methods

Purification of *Mt*UvrAUvrB complex

M. tuberculosis UvrA was over-expressed in *E. coli* BL21 (DE3) strain harboring the plasmid pMtHisUvrA[6]. *M. tuberculosis* UvrB gene was provided by gene synthesis (GenScript) and was over-expressed in *E. coli* BL21 (DE3) strain harboring the plasmid pMtHisUvrB. The two proteins were purified as described in Supplementary information. To obtain the samples used in the cryo-EM experiments, pure *Mt*UvrA- and *Mt*UvrB-containing protein solutions were pooled together in a 1.2 molar excess of *Mt*UvrB and 1 mM ATP and 10 mM $MgCl_2$ were added as stabilizing elements of the complex formation[18,32,33]. The sample mixture was concentrated to 4.3 mg/mL and loaded onto a Superdex 200 Increase 10/300 GL size exclusion chromatography column with a buffer containing 20 mM Tris HCl pH 8.0, 300 mM NaCl. The chromatographic fractions that, on the basis of chromatogram analysis and subsequent SDS-PAGE, contained hetero-tetrameric complexes, were then pooled and concentrated up to 0.5 mg/mL, obtaining the *Mt*UvrA-*Mt*UvrB sample. The *Mt*UvrA-*Mt*UvrB-DNA* was prepared by incubating the *Mt*UvrA-*Mt*UvrB sample with the FLUdT-containing dsDNA (DNA*, Supplementary Table 3), in a 1.2 molar excess of DNA*. The sample was flash-frozen in liquid nitrogen and stored at -80 °C.

The *Mt*UvrA-Δβ-hairpin and *Mt*UvrA-Y323A variants used in the EMSA-, MST- and SPR-based analyses were produced adopting the same procedure used to express and purify the wild type *Mt*UvrA protein, followed by an additional Size Exclusion Chromatographic step using a Superdex 200 Increase 10/300 GL column with a buffer containing 20 mM Tris HCl pH 8.0, 500 mM NaCl, 5% glycerol as the mobile phase.

*Mt*UvrA-*Mt*UvrB DNA complex cryo-EM sample preparation, data collection and data processing

Vitrification of *Mt*UvrA-*Mt*UvrB and *Mt*UvrA-*Mt*UvrB-DNA* samples at 1.75 μM was carried out with a Mark IV Vitrobot (Thermo Fisher Scientific). 3 μl of each sample were applied to a Quantifoil R 1.2/1.3 Cu 300-mesh grid previously glow-discharged at 30 mA for 30" in a GloQube (Quorum Technologies). Immediately after sample application, the grids were blotted in a chamber at 4 °C and 100% humidity, and then plunge-frozen into liquid ethane.

*Mt*UvrA-*Mt*UvrB sample was transferred to a Talos Arctica (Thermo Fisher Scientific) operated at 200 kV equipped with a Falcon III operating in electron counting mode. 3'642 movies were acquired at a nominal magnification of 120'000x corresponding to a pixel size of 0.889 Å/pixel. The total dose was 40 $e^-/Å^2$ equally distributed on 40 frames. Data collection statistics are summarized in Supplementary Table 1.

Movies were preprocessed with RELION 3.1[55] (Supplementary fig. 1). All movies were subjected to motion-correction and dose-weighting using MOTIONCOR2[56]. Estimation of the contrast transfer function (CTF) was performed on aligned dose-weighted sum of power spectra every 4 e^-/A^2 using CTFFIND 4.1.10[57]. Motion-corrected micrographs were imported to WARP and particle picking was preformed using the deep convolutional neural network BoxNet2_20180602 using a particle diameter of 60 Å resulting in a total of 240'304 picked particles. Particles were imported in RELION 3.1 and extracted with a box size of 400×400 pixels and a pixel size of 0.889 Å/pixel, inverted, normalized and imported into CRYOSPARC 4.2.1[58] for further processing. After a first round of 2D classification, particles averages above 60 Å were selected yielding a 148'931 set of particles. The set of particles was further split in two groups depending on their composition through an ab initio job using two models. The two ab initio reconstructed volumes corresponded to *Mt*$UvrA_2$ (68'915 particles) and *Mt*$UvrA_2$-DNA (80'016 particles) and were further cleaned through 3D classification yielding a final number of 22'766 particles and 27'801 particles, respectively. The final resolution of the two structures was 4.9 Å for *Mt*$UvrA_2$ and 4.2 Å for *Mt*$UvrA_2$-DNA, according to an FSC of 0.143 (Supplementary fig. 1). Data processing statistics are summarized in Supplementary Table 1 and a schematic representation of the workflow used is in Supplementary fig. 1.

Vitrified grids of *Mt*UvrA-UvrB-DNA* sample were sent to the CM01 beamline at the ESRF[59,60]) for a data collection. Movies were recorded using a Titan Krios (Thermo Fisher Scientific) operated at 300 kV equipped with a K3 detector operating in electron counting mode. 21'232 movies were acquired from two twin grids at a nominal magnification of 105'000x in superresolution mode bin2 corresponding to a pixel size of 0.84 Å/pixel. The dose rate during movie acquisition was 18.8 e^-/pix/s and the total dose was 40 $e^-/Å^2$ equally distributed on 40 frames. Data collection statistics are summarized in Supplementary Table 1.

Movies were preprocessed with RELION 3.1[55] (Supplementary fig. 5). All movies were subjected to motion-correction and dose-weighting using MOTIONCOR2[56]. Estimation of the CTF was performed on aligned dose-weighted sum of power spectra every 4 e^-/A^2 using CTFFIND 4.1.10[57]. Motion corrected micrographs were imported to WARP and particle picking was preformed using the deep convolutional neural network BoxNet2_20180602 using a particle diameter of 60 Å resulting in a total of 2'158'399 picked particles. Particles were imported in RELION 3.1 and extracted with a box size of 400×400 pixels and a pixel size of 0.84 Å/pixel, inverted, normalized and imported into CRYOSPARC 4.2.1[58] for further processing. After a first round of 2D classification, particles averages above 60 Å were selected yielding 666'671 particles. The set of particles was further split in three groups depending on their composition and an ab initio model was generated with each set. The initial set of 666'671 selected particles was heterogeneous refined using three ab initio models as references. Three classes corresponding to *Mt*$UvrA_2UvrB_2$-DNA* (143'862 particles), *Mt*$UvrA_2UvrB_1$-DNA* (138'164 particles) and *Mt*$UvrA_2$-DNA (242'593 particles) were further cleaned through 2D classification yielding a final number of 110'916, 99'428 and 229'676 particles, respectively. The final resolution for the three structures was 4.0 Å for *Mt*$UvrA_2UvrB_2$-DNA*, 4.3 Å for *Mt*$UvrA_2UvrB_1$-DNA* and 3.2 Å for *Mt*$UvrA_2$-DNA, according to an FSC of 0.143 (Supplementary fig. 6). *Mt*$UvrA_2UvrB_2$-DNA* reconstruction was split in two halves and each applied on the full reconstruction for particle subtraction first, and then the complementary half on the subtracted particles for a local refinement. The half reconstruction of the *Mt*$UvrA_2UvrB_2$-DNA* produced a map at 3.6 Å and 3.7 Å of resolution. The two halves were merged in a composite map using chimera[61]. Data processing statistics are summarized in Supplementary Table 1 and a schematic representation of the workflow used is in Supplementary fig. 5.

Model building and refinement

For *Mt*$UvrA_2$-DNA, a previously published structure of *Tm*UvrA (PDB: 3PIH) was used as initial model. UCSF Chimera[61] was used to rigidly fit the model in the density map. The changes in sequence and conformations were made using Coot[62]. The Insertion Domains of

*Mt*UvrA crystal structure (PDB: 3ZQJ) were rigid-body fit into the map, with the exception of the non-modeled β hairpin domains, and the model was then refined against the map using Phenix Real Space Refine[63]. A random nucleotide sequence of DNA was modeled and a density fit restraining the Watson-Crick base pairs ad the Pi-stacking between nucleobases was performed. Nevertheless, the electron density map signal of one DNA strand fades away in the central portion and for this reason only a single strand was modeled there. Starting from this configuration, we parameterized *Mt*UvrA$_2$-DNA in the AMBER14SB[64] force field with OL15 torsional modifications[65] for DNA using the tleap program. The zinc ions coordination has been modeled via the ZAFF force field[66]. We parameterized ADP via the GAFF2 force field and computed its point charges using the AM1-BCC semiempirical approach. Subsequently, we solvated it with the OPC water model[67] and neutralized with sodium ions. This system underwent a two-phases energy minimization (steepest descent with a 1000 kJ/mol energy tolerance and conjugate gradient minimization with a 100 kJ/mol energy tolerance) using GROMACS 2022.3[68], obtaining the final model. Figures were prepared with CHIMERAX[69], PYMOL[70], INKSCAPE[71] and BIORENDER[72].

For *Mt*UvrA$_2$UvrB$_1$-DNA*, the *Mt*UvrA$_2$-DNA structure and the chain corresponding to UvrB from a previously published model (PDB: 3UWX) was docked into the map, manually adjusted in Coot[62] and refined using Phenix Real Space Refine[63].

For the *Mt*UvrA$_2$UvrB$_2$-DNA* structure, the previously published model (PDB: 3UWX) was used and a rigid-body fit was applied in order to get the final model, finally refined using Phenix Real Space Refine[63]. In analogy with the modeling performed for *Mt*UvrA$_2$-DNA, for *Mt*UvrA$_2$UvrB$_2$-DNA* we parameterized the system with the AMBER14SB-OL15-ZAFF force field and solvated it with OPC water and neutralized with sodium ions. We obtained the final model with the same two-phases minimization algorithm used in *Mt*UvrA$_2$-DNA refinement.

Plasmid vectors for the over-expression of the *Mt*UvrA variants in *E. coli* cells

We generated the plasmid vector that encodes the *M*tUvrA-Y323A variant by using the pMtHisUvrA[6] construct as the DNA template, the primers pair Y323Afor/Y323Arev (see Supplementary Table 3), and the QuikChange II site-directed mutagenesis kit (Stratagene). The protein-encoding open reading frame in the resulting construct was verified by sequencing (Eurofins MWG Operon).

The expression construct for *Mt*HisUvrA-Δβ-hairpin was provided by a custom gene synthesis service (GenScript), encoding the protein variant that lacks the Q361-E381 spanning region, corresponding to the entire ID β-hairpin.

DNA substrates

Mutagenic primers and DNA oligonucleotides used in biochemical assays and structural investigation, synthesized by Eurofins Genomics, are reported in Supplementary Table 3.

Dot Blot Assay

All samples were treated with 0.4 M NaOH, 10 mM EDTA pH8 to denature DNA, boiled for 10 min at 94 °C and finally neutralized with 2 M $NH_4CH_3COO^-$ 1:1 v/v. DNA was then loaded on a nitrocellulose membrane activated with 6X SSC buffer through a Dot Blot vacuum manifold (SRC 96 Schleicher and Schuell), followed by two washes with 2X SSC. The membrane was dried, and DNA/membrane were cross-linked for 2 h at 80 °C.

The membrane was then blocked and hybridized with primary antibodies (anti-6-4PPs clone 64M-2; anti-CPDs clone TDM-2; anti-8-oxo-dG (15A3) sc-66036; anti-ssDNA MAB3034) and secondary antibodies HRP-conjugated. Chemiluminescence reaction was induced using Bio-Rad Clarity ECL and developed with Chemidoc Touch (Bio-Rad). SH-SY5Y (ATCC-CRL-2266) cells were untreated or treated with UVC lamp, and then harvested. Genomic DNA was purified using Macherey-Nagel™ NucleoSpin™ Tissue kit, processed as the UvrA sample and loaded on nitrocellulose with serial dilution (125 ng, 62 ng, 31 ng).

Antibody sources and working concentrations are reported: Anti-CPDs TDM-2 (D194-1): CosmoBio, monoclonal, Mouse, 1:1000. Anti-6-4PP (64M2): CosmoBio, monoclonal, Mouse, 1:500. Anti- ssDNA (MAB3034): Merck-Millipore, monoclonal, Mouse, 1:1000. Anti-8OHdG (15A3), Santa Cruz Biotechnology sc-66036, monoclonal, Mouse 1:3000 in 3% BSA. Goat anti-Mouse IgG (H + L): ThermoFisher Scientific, Secondary Antibody HRP (Cat # 31430), 1:10000. All of them were used diluted in TBS 0.1% Tween-20.

Electrophoretic mobility shift assays (EMSA)

A biotinylated dsDNA fragment, containing 2 fluorescein-modified thymine nucleobases (FLUdT) and 5′-protruding ends, was mixed, at a fixed 0.15 μM concentration, with increasing concentrations (0.0-1.5 μM) of wild type *Mt*UvrA, or *Mt*UvrA-Y323, or *Mt*UvrA-Δβ-hairpin, in binding buffer (50 mM Tris HCl pH 8.0, 500 mM NaCl, 5% glycerol; final volume=20 μL). Upon a 5 min incubation at 25 °C, samples were electrophoresed on 8% polyacrylamide gel (in 44.5 mM Tris, 44.5 mM boric acid, 1 mM EDTA, pH 8.3) at 100 V for 30 min. The bands were visualized by direct gel imaging using a green light-emitting diode (LED)/605-nm-band-pass filter excitation/emission parameters, respectively.

Surface Plasmon Resonance analysis

A Biacore X100 (GE Healthcare) instrument was used for DNA binding experiments. The biotinylated dsDNA fragment containing 2 fluorescein molecules was immobilized onto the surface of a SA sensor chip (cat # BR100012, GE Healthcare), functionalized with streptavidin; the DNA was immobilized onto the active flow cell (#2), while the other flow cell was used as a reference. Recombinant UvrA proteins (wild type and mutant versions) were diluted to a concentration of 50 nM in HBS-EP+ buffer (GE Healthcare). Considering molecular weights (MW) of ligand and analytes of about 25 kDa and 109 kDa respectively, the appropriate ligand density (RL) on the chip was calculated according to the following equation: RL = (ligand MW/analyte MW) × Rmax × (1/Sm), where Rmax is the maximum binding signal (200 RUs) and Sm corresponds to the binding stoichiometry DNA:protein that is 1:2. Accordingly, the target capture level of the oligonucleotides was of 20 response units (RUs). Increasing concentrations of UvrA proteins were flowed over the SA sensor chip coated with damages dsDNA at a flow rate of 30 μl/min at 25 °C with an association time of 120 s and a dissociation phase of 600 s. A double regeneration step with 50 mM Glycine pH 1.5 and 0.4% SDS was performed following each analytic cycle.

The affinity constant (K_D) and the kinetic parameters were evaluated using the BIAcore evaluation software (GE Healthcare) and the reliability of the kinetic constants calculated by assuming a heterogeneous ligand model supported by the quality assessment indicators values.

MicroScale Thermophoresis

DNA-binding studies were also performed using MicroScale Thermophoresis (MST) according to previously described methods[72,73]. Damaged dsDNA fragment was used as the probe and intrinsic fluorescence of the two fluorescein molecules was used to avoid the labeling. Damaged dsDNA was used at a concentration of 10 nM and the ligands (UvrA wild type and mutated proteins) were diluted, starting from the highest concentration of 1 μM, in 50 mM Tris HCl pH 8, 300 mM NaCl, 5% glycerol; measurements were performed using Premium standard-treated glass capillaries and the instrument Monolith NT.115 (Nano-Temper Technologies). The IR laser-power was set to 40/80% the laser on-and-off times were set at 20 and 5 s, respectively. The amplitude normalized data ΔFnorm of each dataset

were averaged and plotted against the concentration of the unlabeled ligand on a logarithmic scale. The binding data were analyzed using MO affinity analysis software, as provided by the manufacturer.

Reporting summary

Further information on research design is available in the Nature Portfolio Reporting Summary linked to this article.

Data availability

The density maps and atomic coordinates reported in this paper have been deposited in the Electron Microscopy Data Bank (EMDB) and RCSB Protein Data Bank (RCSB PDB), respectively, with accession codes as follows: DNA-free *Mt*UvrA$_2$ dimer structure EMD-51169 and PDB ID 9GA2; *Mt*UvrA$_2$ bound to endogenous *E. coli* DNA at low resolution EMD-51168; *Mt*UvrA$_2$UvrB$_1$ bound to damaged oligonucleotide EMD-51170 and PDB ID 9GA3; *Mt*UvrA$_2$UvrB$_2$ bound to damaged oligonucleotide (half 1) EMD-51171; *Mt*UvrA$_2$UvrB$_2$ bound to damaged oligonucleotide (half 2) EMD-51172; *Mt*UvrA$_2$UvrB$_2$ bound to damaged oligonucleotide EMD-51173 and PDB ID 9GA4; *Mt*UvrA2 bound to endogenous *E. coli* DNA EMD-51174 and PDB ID 9GA5. The movies were deposited in EMPIAR[74,75] under the ascension code: EMPIAR-12274. Source data are provided with this paper.

References

1. Kisker, C., Kuper, J. & Van Houten, B. Prokaryotic nucleotide excision repair. *Cold Spring Harb. Perspect. Biol.* **5**, a012591 (2013).
2. Truglio, J. J., Croteau, D. L., Van Houten, B. & Kisker, C. Prokaryotic Nucleotide Excision Repair: The UvrABC System. *Chem. Rev.* **106**, 233–252 (2006).
3. Wozniak, K. J., & Simmons, L. A. Bacterial DNA excision repair pathways. *Nat. rev. Microbiol.* **20**, 465–477 (2022).
4. Warner, D. F. The role of DNA repair in M. tuberculosis pathogenesis, *Drug Discov. Today: Disease Mechan.* **7**, e5–e11 (2010).
5. Pakotiprapha, D., Samuels, M., Shen, K., Hu, J. H. & Jeruzalmi, D. Structure and mechanism of the UvrA-UvrB DNA damage sensor. *Nat. Struct. Mol. Biol.* **19**, 291–298 (2012).
6. Rossi, F. et al. The biological and structural characterization of Mycobacterium tuberculosis UvrA provides l insights into its mechanism of action. *Nucleic Acids Res* **39**, 7316–7328 (2011).
7. Jaciuk, M., Nowak, E., Skowronek, K., Tańska, A. & Nowotny, M. Structure of UvrA nucleotide excision repair protein in complex with modified DNA. *Nat. Struct. Mol. Biol.* **18**, 191–198 (2011).
8. Timmins, J. et al. Structural and Mutational Analyses of Deinococcus radiodurans UvrA2 Provide Insight into DNA Binding and Damage Recognition by UvrAs. *Structure* **17**, 547–558 (2009).
9. Kraithong, T., Hartley, S., Jeruzalmi, D. & Pakotiprapha, D. A peek inside the machines of bacterial nucleotide excision repair. *Int. J. Mol. Sci.* **22**, 1–20 (2021).
10. Pakotiprapha, D. et al. Crystal Structure of Bacillus stearothermophilus UvrA Provides Insight into ATP-Modulated Dimerization, UvrB Interaction, and DNA Binding. *Mol. Cell* **29**, 122–133 (2008).
11. Lahiri, S., Rizzi, M., Rossi, F. & Miggiano, R. Mycobacterium tuberculosis UvrB forms dimers in solution and interacts with UvrA in the absence of ligands. *Proteins: Struct., Funct. Bioinforma.* **86**, 98–109 (2018).
12. Lee, S. J., Sung, R. J., & Verdine, G. L. Mechanism of DNA Lesion Homing and Recognition by the Uvr Nucleotide Excision Repair System. *Research* 5641746 (Washington, D.C., 2019). https://doi.org/10.34133/2019/5641746.
13. DellaVecchia, M. J. et al. Analyzing the handoff of DNA from UvrA to UvrB utilizing DNA-protein photoaffinity labeling. *J. Biol. Chem.* **279**, 45245–45256 (2004).
14. Truglio, J. J. et al. Structural basis for DNA recognition and processing by UvrB. *Nat. Struct. Mol. Biol.* **13**, 360–364 (2006).
15. Thakur, M., Kumar, M. B. J. & Muniyappa, K. Mycobacterium tuberculosis UvrB Is a Robust DNA-Stimulated ATPase That Also Possesses Structure-Specific ATP-Dependent DNA Helicase Activity. *Biochemistry* **55**, 5865–5883 (2016).
16. Stracy, M. et al. Single-molecule imaging of UvrA and UvrB recruitment to DNA lesions in living Escherichia coli. *Nat. Commun.* **7**, 12568 (2016).
17. Sancar, A. & Hearst, J. E. *Mol. Matchmakers. Sci. (1979)* **259**, 1415–1420 (1993).
18. Pakotiprapha, D. & Jeruzalmi, D. Small-angle X-ray scattering reveals architecture and A2B2 stoichiometry of the UvrA-UvrB DNA damage sensor. *Proteins: Struct., Funct. Bioinforma.* **81**, 132–139 (2013).
19. Jaciuk, M. et al. A combined structural and biochemical approach reveals translocation and stalling of UvrB on the DNA lesion as a mechanism of damage verification in bacterial nucleotide excision repair. *DNA Repair (Amst)* **85**, 102746 (2020).
20. Kad, N. M., Wang, H., Kennedy, G. G., Warshaw, D. M. & Van Houten, B. Collaborative Dynamic DNA Scanning by Nucleotide Excision Repair Proteins Investigated by Single- Molecule Imaging of Quantum-Dot-Labeled Proteins. *Mol. Cell* **37**, 702–713 (2010).
21. Ghodke, H., Ho, H. N. & van Oijen, A. M. Single-molecule live-cell imaging visualizes parallel pathways of prokaryotic nucleotide excision repair. *Nat. Commun.* **11**, 1477 (2020).
22. Pakotiprapha, D., Liu, Y., Verdine, G. L. & Jeruzalmi, D. A structural model for the damage-sensing complex in bacterial nucleotide excision repair. *J. Biol. Chem.* **284**, 12837–12844 (2009).
23. Zou, Y. & Van Houten, B. *Strand Opening by the UvrA 2 B Complex Allows Dynamic Recognition of DNA Damage. EMBO J.* **18** (1999).
24. Verhoeven, E. E. A. Architecture of nucleotide excision repair complexes: DNA is wrapped by UvrB before and after damage recognition. *EMBO J.* **20**, 601–611 (2001).
25. Orren D. K. & Sancar A. The (A)BC excinuclease of Escherichia coli has only the UvrB and UvrC subunits in the incision complex. *Proc Natl Acad Sci USA.* **86**, 5237–5241 (1989).
26. Warner D. F., Tønjum T. & Mizrahi V. DNA metabolism in mycobacterial pathogenesis. *Curr Top Microbiol Immunol.* **374**, 27–51 (2013).
27. Darwin, K. H. & Nathan, C. F. Role for Nucleotide Excision Repair in Virulence of *Mycobacterium tuberculosis*. *Infect. Immun.* **73**, 4581–4587 (2005).
28. Kelly, M. C., Whitaker, G., White, B. & Smyth, M. R. Nickel(II)-catalysed oxidative guanine and DNA damage beyond 8-oxoguanine. *Free Radic. Biol. Med* **42**, 1680–1689 (2007).
29. Sagendorf J. M., Markarian N., Berman H. M. & Rohs R. DNAproDB: an expanded database and web-based tool for structural analysis of DNA-protein complexes. *Nucleic Acids Res.* **48**, D277–D287 (2020).
30. Sagendorf, J. M., Berman, H. M. & Rohs, R. DNAproDB: an interactive tool for structural analysis of DNA–protein complexes. *Nucleic Acids Res* **45**, W89–W97 (2017).
31. Li, S., Olson, W. K. & Lu, X.-J. Web 3DNA 2.0 for the analysis, visualization, and modeling of 3D nucleic acid structures. *Nucleic Acids Res* **47**, W26–W34 (2019).
32. Colizzi, F. et al. Asymmetric base-pair opening drives helicase unwinding dynamics. *Proc. Natl Acad. Sci.* **116**, 22471–22477 (2019).
33. Voter, A. F., Qiu, Y., Tippana, R., Myong, S. & Keck, J. L. A guanine-flipping and sequestration mechanism for G-quadruplex unwinding by RecQ helicases. *Nat. Commun.* **9**, 4201 (2018).
34. Marians, K. J. Crawling and Wiggling on DNA. *Structure* **8**, R227–R235 (2000).
35. Tubbs, J. L., Pegg, A. E. & Tainer, J. A. DNA binding, nucleotide flipping, and the helix-turn-helix motif in base repair by O6-alkylguanine-DNA alkyltransferase and its implications for cancer chemotherapy. *DNA Repair (Amst.)* **6**, 1100–1115 (2007).

36. Hollis, T., Ichikawa, Y. & Ellenberger, T. DNA bending and a flip-out mechanism for base excision by the helix–hairpin–helix DNA glycosylase, Escherichia coli AlkA. *EMBO J.* **19**, 758–766 (2000).
37. Demple, B. Enzyme Structures: DNA repair flips out. *Curr. Biol.* **5**, 719–721 (1995).
38. Gade, P. et al. Structural and functional analyses of the echinomycin resistance conferring protein Ecm16 from Streptomyces lasalocidi. *Sci. Rep.* **13**, 7980 (2023).
39. Wagner, K., Moolenaar, G. F. & Goosen, N. Role of the insertion domain and the zinc-finger motif of Escherichia coli UvrA in damage recognition and ATP hydrolysis. *DNA Repair (Amst.)* **10**, 483–496 (2011).
40. Charman, R. J. & Kad, N. M. Single molecule iSCAT imaging reveals a fast, energy efficient search mode for the DNA repair protein UvrA. *Nanoscale* **14**, 5174–5184 (2022).
41. Smith, B. T., Grossman, A. D. & Walker, G. C. Localization of UvrA and Effect of DNA Damage on the Chromosome of *Bacillus subtilis*. *J. Bacteriol.* **184**, 488–493 (2002).
42. Kraithong, T. et al. Real-time investigation of the roles of ATP hydrolysis by UvrA and UvrB during DNA damage recognition in nucleotide excision repair. *DNA Repair (Amst)* **97**, 103024 (2021).
43. Eryilmaz, J. et al. Structural insights into the cryptic DNA-dependent ATPase activity of UvrB. *J. Mol. Biol.* **357**, 62–72 (2006).
44. Waters, T. R., Eryilmaz, J., Geddes, S. & Barrett, T. E. Damage detection by the UvrABC pathway: Crystal structure of UvrB bound to fluorescein-adducted DNA. *FEBS Lett.* **580**, 6423–6427 (2006).
45. Grossman, L. & Yeung, A.T. The UvrABC endonuclease of Escherichia coli. *Photochemistry and Photobiology*, **51**, 749–755 (1990).
46. Mazur, S. J. & Grossman, L. Dimerization of Escherichia coli UvrA and its binding to undamaged and ultraviolet light damaged DNA. *Biochemistry* **30**, 4432–4443 (1991).
47. Zou, Y. Strand opening by the UvrA2B complex allows dynamic recognition of DNA damage. *EMBO J.* **18**, 4889–4901 (1999).
48. Zou, Y., Walker, R., Bassett, H., Geacintov, N. E. & Van Houten, B. Formation of DNA Repair Intermediates and Incision by the ATP-dependent UvrB-UvrC Endonuclease. *J. Biol. Chem.* **272**, 4820–4827 (1997).
49. Gordienko, I. UvrAB activity at a damaged DNA site: is unpaired DNA present? *EMBO J.* **16**, 880–888 (1997).
50. Shi, Q., Thresher, R., Sancar, A. & Griffith, J. Electron microscopic study of (A)BC excinuclease. *J. Mol. Biol.* **226**, 425–432 (1992).
51. Wang, H. et al. DNA wrapping is required for DNA damage recognition in the Escherichia coli DNA nucleotide excision repair pathway. *Proc. Natl Acad. Sci. USA* **106**, 12849–12854 (2009).
52. Scrima, A. et al. Structural Basis of UV DNA-Damage Recognition by the DDB1-DDB2 Complex. *Cell* **135**, 1213–1223 (2008).
53. Chen, X. et al. Kinetic gating mechanism of DNA damage recognition by Rad4/XPC. *Nat. Commun.* **6**, 5849 (2015).
54. Paul, D. et al. Tethering-facilitated DNA 'opening' and complementary roles of β-hairpin motifs in the Rad4/XPC DNA damage sensor protein. *Nucleic Acids Res* **48**, 12348–12364 (2021).
55. Zivanov, J., Nakane, T. & Scheres, S. H. W. Estimation of high-order aberrations and anisotropic magnification from cryo-EM data sets in *RELION* -3.1. *IUCrJ* **7**, 253–267 (2020).
56. Zheng, X. et al. Mechanism of ligand activation of a eukaryotic cyclic nucleotide–gated channel. *Nat. Struct. Mol. Biol.* **27**, 625–634 (2020).
57. Rohou, A. & Grigorieff, N. CTFFIND4: Fast and accurate defocus estimation from electron micrographs. *J. Struct. Biol.* **192**, 216–221 (2015).
58. Punjani, A., Rubinstein, J. L., Fleet, D. J. & Brubaker, M. A. cryoSPARC: algorithms for rapid unsupervised cryo-EM structure determination. *Nat. Methods* **14**, 290–296 (2017).
59. Kandiah, E. et al. CM01: a facility for cryo-electron microscopy at the European Synchrotron. *Acta Crystallogr D. Struct. Biol.* **75**, 528–535 (2019).
60. Sanjuan, A. C. & Miggiano, R. Italian CryoEM Bag (ICB) [dataset]. European Synchrotron Radiation Facility. https://doi.org/10.15151/ESRF-ES-893681585 (2025).
61. Pettersen, E. F. et al. UCSF Chimera—A visualization system for exploratory research and analysis. *J. Comput Chem.* **25**, 1605–1612 (2004).
62. Emsley, P., Lohkamp, B., Scott, W. G. & Cowtan, K. Features and development of *Coot*. *Acta Crystallogr D. Biol. Crystallogr* **66**, 486–501 (2010).
63. Afonine, P. V. et al. Real-space refinement in *PHENIX* for cryo-EM and crystallography. *Acta Crystallogr D. Struct. Biol.* **74**, 531–544 (2018).
64. Maier, J. A. et al. ff14SB: Improving the Accuracy of Protein Side Chain and Backbone Parameters from ff99SB. *J. Chem. Theory Comput* **11**, 3696–3713 (2015).
65. Galindo-Murillo, R. et al. Assessing the Current State of Amber Force Field Modifications for DNA. *J. Chem. Theory Comput* **12**, 4114–4127 (2016).
66. Peters, M. B. et al. Structural Survey of Zinc-Containing Proteins and Development of the Zinc AMBER Force Field (ZAFF). *J. Chem. Theory Comput* **6**, 2935–2947 (2010).
67. Izadi, S., Anandakrishnan, R. & Onufriev, A. V. Building Water Models: A Different Approach. *J. Phys. Chem. Lett.* **5**, 3863–3871 (2014).
68. Abraham, M. J. et al. GROMACS: High performance molecular simulations through multi-level parallelism from laptops to supercomputers. *SoftwareX* **1–2**, 19–25 (2015).
69. Meng, E. C. et al. UCSF ChimeraX: Tools for structure building and analysis. *Protein Sci.* **32**, e4792 (2023).
70. Schrödinger, L., & DeLano, W. (2020). *PyMOL*. Retrieved from http://www.pymol.org/pymol
71. Inkscape Project. (2020). Inkscape. Retrieved from https://inkscape.org.
72. Duhr S. & Braun D. Why molecules move along a temperature gradient. *Proc Natl Acad Sci USA*. **103**, 19678–19682 (2006).
73. Wienken, C. J., Baaske, P., Rothbauer, U., Braun, D. & Duhr, S. Protein-binding assays in biological liquids using microscale thermophoresis. *Nat. Commun.* **1**, 100 (2010).
74. Correction to 'EMPIAR: The Electron Microscopy Public Image Archive'. *Nucleic Acids Res* **51**, 3499–3499 (2023).
75. Iudin, A. et al. EMPIAR: the Electron Microscopy Public Image Archive. *Nucleic Acids Res* **51**, D1503–D1511 (2023).

Acknowledgements

We acknowledge the European Synchrotron Radiation Facility for provision of beam time on CM01 and we would like to thank Dr. Eaazhisai Kandiah for assistance. Part of the cryo-EM experiments were carried out at the NoLimits center of the University of Milan. This research was supported by Fondazione Cariplo (grant n. 2016–0604 received by R.M.) and by the Italian Ministry of University and Research with the call PRIN 2022 PNRR (grant n. P2022P8KMF received by R.M. and A.C.S.). The authors would like to thank all the students of the FREE-MOVER project of the University of Piemonte Orientale for the fruitful discussion of the scientific data included in the manuscript.

Author contributions

R.M. and A.C.S. and D.J. conceptualized the experiments. M.G. and G.F. purified the recombinants proteins for biochemical assays and cryo-EM experiments. M.G., R.M., A.C.S., F.R. and M.R. performed and analyzed the biochemical experiments including surface plasmon resonance, EMSA and microscale thermophoresis. D.R. and S.S. performed dot blot assay and DNA damage quantification. M.G. and A.C.S. performed cryo-

EM sample preparation and validation. M.G. and A.C.S. processed and analyzed the cryo-EM datasets. M.G., A.C.S., M.B. and R.C. performed model building and refinement. M.G., R.M. and A.C.S. wrote the manuscript with input from D.J., F.R. and M.B.

Competing interests
The authors declare no competing interests.

Additional information
Supplementary information The online version contains supplementary material available at https://doi.org/10.1038/s41467-025-58670-0.

Correspondence and requests for materials should be addressed to Antonio Chaves-Sanjuan or Riccardo Miggiano.

Peer review information *Nature Communications* thanks the anonymous reviewer(s) for their contribution to the peer review of this work. A peer review file is available.